



Synthesis optimization and investigation on electrical properties of Fe⁺²-doped Mg₂TiO₄ ceramics for energy storage

Rupali Singh¹ · K. Biswas¹

Received: 14 February 2020 / Accepted: 11 June 2020 / Published online: 18 June 2020
© Springer Science+Business Media, LLC, part of Springer Nature 2020

Abstract

Polycrystalline MgFeTiO₄ ceramic is prepared using a solid-state reaction route. The structural, vibrational, morphology, and electrical characteristics of the compound are studied. Crystal structure and phase analysis results suggest that MgFeTiO₄ has a cubic spinel structure corresponding to the Fd3m space group. Fourier transform infrared (FTIR) and Raman spectroscopy indicate that Mg–O, Fe–O, and Ti–O bonds are present in the sample. X-ray photoelectron spectroscopy study suggests the valence state of iron (Fe); thus, the formation of MgFeTiO₄ is confirmed. The morphology and compositional analyses are done by field emission scanning electron microscopy and high-resolution transmission electron microscopy. The electrical and dielectric behaviors of the sample are studied at various temperature ranges. The dc conductivity of $5.68 \times 10^{-4} \text{ S cm}^{-1}$ is obtained at 300 °C, which is higher compared to LiFeTiO₄. The activation energy is estimated and observed two different temperature-dependent conductivity regions.

1 Introduction

Currently, renewable energy sources viz., the solar, wind, and geothermal are becoming very popular due to the shortage of traditional fossil fuels and crude oil sources [1–4]. The evolution and research in the area of storage devices like rechargeable batteries (Li/Na/Mg-ion) are escalating for storing the energy. Li-ion battery technology is well established among storage devices due to its high energy conversion efficiency, long cycle life, and low self-discharge [5, 6]. Based on the literature [7], it is found that the working principle of Li/Na/Mg-ion rechargeable batteries is the same. The cathode-storing ions by electrochemical intercalation should possess an apt number of lattice positions to store and eject working ions reversibly [7]. Although progress in Li-ion batteries occurred extensively, the major problem in lithium batteries is the dendrite formation, which causes an internal short circuit and fire hazard. Moreover, it is expensive, unsafe, and there are growing environmental concerns as well [8–10]. Therefore, the development of new electrochemical storage systems using safe, green, and low-cost electrode materials with high theoretical capacities are in the

research forefront [11]. Magnesium metal's higher volumetric capacity in comparison to lithium metal (i.e., 3832 mAh cm⁻³ for Mg vs. 2061 mAh cm⁻³ for Li [12–14]) is gripping attention. Moreover, Mg deliberates low electrode potential, high charge density, and reasonable low-cost batteries owing to the fact that it is the most abundant natural element on earth's crust [9, 12–16].

Although Mg has many advantages over Li, still Mg-ion batteries have several issues like high potential cathode material, high-voltage stable electrolyte, and many more. To overcome these issues, the researcher is trying to develop a new cathode system. The reported cathode materials are Chevrel phases (CP) (Mg_xMo₆T₈; T = S, Se, Te) [17–19], Mixed Chevrel phases (Mo₆S_{8-y}Se_y; y = 1,2) [20] and Cu_xMo₆S₈ (x = 1) [21], layered (TiS₂, V₂O₅, V₆O₁₃) [22, 23], transition metal oxides (TMO), defect oxide spinel, olivine compound (MgMSiO₄ (M = Mn, Co, Fe) [15, 24, 25], MT₂ (M = metal, T = S, Se), magnesium–sulphur (Mg–S) [10], etc. Spinel structure-based magnesium cathode may show high potential and high capacity, but there are very few spinel-based Mg cathode materials. The spinel type of the cathode shows many advantages in LIBs. It is not only pure ionic conductor but also a mixed conductor. Spinel LiFeTiO₄ with two redox reaction centres, viz; Fe³⁺/Fe²⁺ and Ti⁴⁺/Ti³⁺ and shows better electronic conductivity [26].

The titanium-based oxides are widely used in electrode material because of abundance, excellent electrochemical

✉ Rupali Singh
rupali18feb@gmail.com

¹ Department of Metallurgical and Materials Engineering,
Indian Institute of Technology, Kharagpur 721302, India

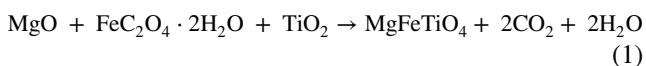
stability, development of less strain during intercalation/deintercalation, prolonged cyclability, and lower cost [27, 28]; but they have poor electrical conductivity ($\sim 10^{-12}$ and 10^{-13} S cm $^{-1}$) [27]. To improve these properties, the transition metals (Fe $^{3+}$, Mn $^{3+}$, Co $^{3+}$, Ni $^{2+}$, etc.) or non-metal are doped in the Mg or Ti sites. The structural and electrical properties of Mg $_2$ TiO $_4$ are already reported [29], but in the absence of redox ion, it is electrochemically inactive. By incorporating the transition metals, the electrochemical properties can be improved.

In the present work, a new Mg-based spinel structure viz, MgFeTiO $_4$, is selected as possible electrode material for the Mg-ion battery. The concept is borrowed from the well-studied LiFeTiO $_4$, which shows mixed conduction. LiFeTiO $_4$ shows the electronic conductivity of the order of 10^{-6} S cm $^{-1}$ at 350 °C due to the presence of more than one redox center per atom. The high-specific capacitance, near-perfect Columbia efficiency, and remarkable electrochemical properties had been reported for LiFeTiO $_4$ [26, 30]. In view of that, MgFeTiO $_4$ is synthesized by using a solid-state reaction route and subsequently structural, vibrational, electrical characterizations of the same were examined.

2 Experimental method

2.1 Preparation of spinel MgFeTiO $_4$

MgFeTiO $_4$ was prepared via solid-state reaction route using magnesium oxide (Loba Chemie, 98%), iron oxalate (Alfa Aesar, 99%), and titanium dioxide (Loba Chemie, 99%) as raw materials. The raw materials were mixed for 6 h with a stoichiometric ratio of 1:1:1 followed by 12 h of calcination at various temperatures in an argon atmosphere to form the MgFeTiO $_4$ as per the following reaction:



2.2 Structural characterization technique

The thermogravimetric analysis of the as-synthesized sample was performed using Perkin Elmer Pyris Diamond TG–DTA analyzer. XRD of the sample was done using BRUKER D8 Advance, Germany, with diffraction angles ranging from 15° to 80° using CuK $_{\alpha}$ radiation. Rietveld refinement was performed with software TOPAS. Rietveld refinement is done using isostructural LiFeTiO $_4$ by replacing Li with Mg. Fourier transform infrared (FTIR) spectra of the powder sample was obtained using Thermofisher Scientific NICOLET 6700 FTIR spectrometer using a KBr pellet technique in the wavenumber range between 400 and 4000 cm $^{-1}$. Raman spectrum of powder sample was obtained at room

temperature using Raman Optical Microscope, Olympus, BX41 in the wavenumber region of 100 to 1000 cm $^{-1}$. X-ray photoelectron spectroscopy (XPS) analysis was carried out by PHI5000 Versa Probe II system (ULVAC–PHI, INC) JAPAN. The excitation source was Al K $_{\alpha}$ (1486.6 eV) with the hemispherical analyzer and a multichannel detector. The particle morphology and elemental mapping of the powder were observed using a field emission scanning electron microscopy (FESEM) obtained by ZEISS EVO 60 and high-resolution transmission electron microscopy (HRTEM, JEOL, JEM-2100F).

2.3 Electrical characterization technique

Detailed investigation of electrical properties of the electrode material was carried out with the aid of complex impedance spectroscopy (CIS). Nature of the conducting system and electrical conductivity of sample was determined with the help of CIS. This technique helps to separate individual contributions of bulk, grain boundary, and electrode polarization effect for a polycrystalline ceramic [31, 32]. The impedance study was executed with HIOKI 3532–50 LCR Hitester at various frequencies ranging from 50 Hz to 5 MHz and at different temperatures (room temperature to 300 °C) at 20 °C intervals. The pellets of the sample before CIS measurement were sintered at 950 °C for 12 h. The silver paste was applied on both sides of this sintered pellets as a current collector. In CIS, the single semi-circular arc may be a combination of two or more arcs. To identify this, the experimental curve was deconvoluted using ZSimp Win software (described in Sect. 3.2).

3 Results and discussion

3.1 Structural characterizations of synthesized MgFeTiO $_4$

The thermal analysis of as-synthesized powder is shown in Fig. 1a and observed that its decomposition occurs in multiple stages. The first weight loss between 150 and 200 °C is due to the dehydration of surface-absorbed moisture in the sample. The endothermic peak confirms this weight loss at 200 °C in the DTA curve [33, 34]. The second weight loss between 200 and 350 °C is attributed to vaporization of chemisorbed (i.e., structural) water; the exothermic peak is assigned and the third weight loss between 350 and 500 °C is due to the decomposition of carbonaceous compound present in physical mixture of the precursors [30, 32]. The TGA–DTA curve exhibits no change in mass occurs after 500 °C. The exothermic peak around 1100 °C is due to decomposition of MgFeTiO $_4$ into FeTiO $_3$ which shows the transition from MgFeTiO $_4$ into FeTiO $_3$ crystalline form [35].

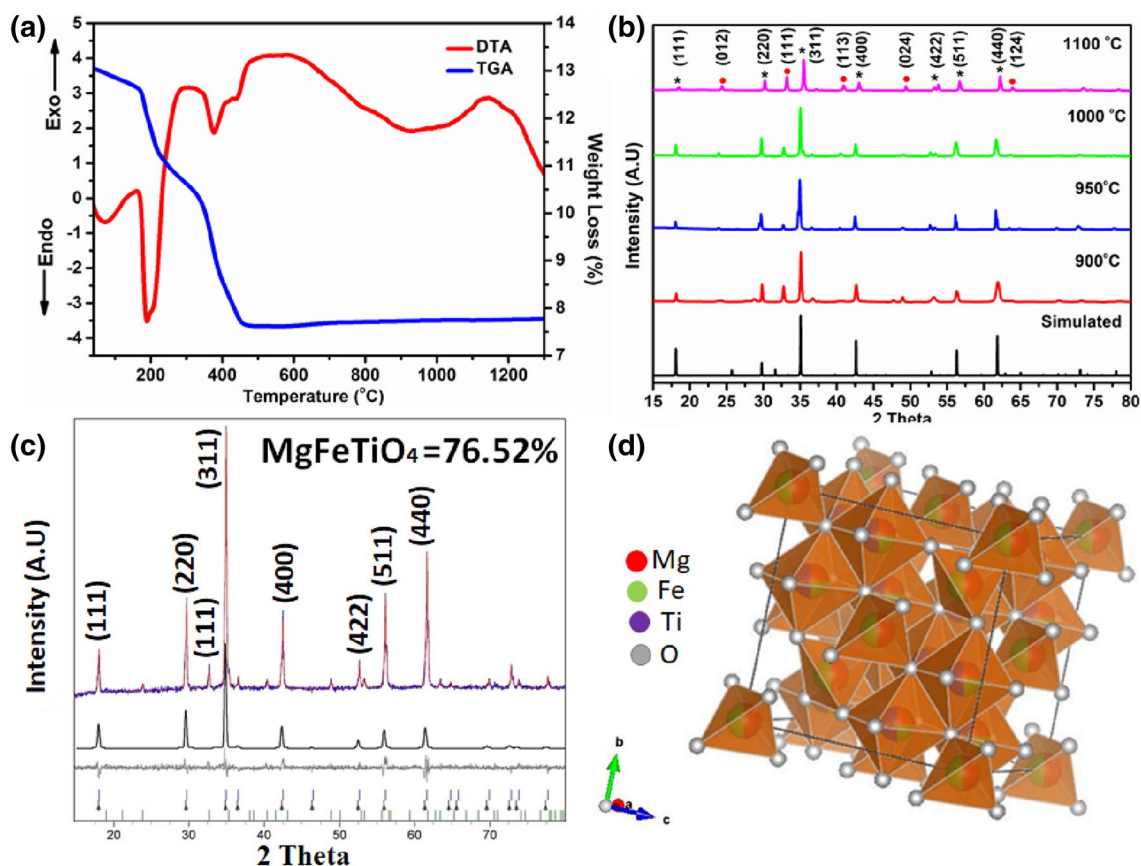


Fig. 1 a DTA–TGA curve of MgFeTiO_4 up to temperature 1300 °C, b XRD patterns of MgFeTiO_4 experimental calcined at different temperatures and simulated (* $\text{MgFeTiO}_4/\text{Fe}_2\text{TiO}_4 \cdot \text{FeTiO}_3$), c Rietveld

analysis of MgFeTiO_4 , d Crystal structure of MgFeTiO_4 spinel generated by VESTA

The phase purity and crystal structural analysis of MgFeTiO_4 calcined at 900, 950, 1000, 1100 °C are shown in Fig. 1b. Formation of MgFeTiO_4 is confirmed along with some traces of other phases. With increased temperature, the intensity of other phases are increasing, suggesting a possible decomposition. Hence, sample calcined at 950 °C is selected for further examination. The experimental XRD pattern of MgFeTiO_4 matches well with that of the simulated one shown in Fig. 1c (obtained from structure simulated by density functional theory (DFT)). The DFT simulation is done by using LiFeTiO_4 isostructural of MgFeTiO_4 and GGA-PBE exchange–correlation functional with $4 \times 4 \times 4$ k-point mesh was used for simulation. In LiFeTiO_4 structure, Li is replaced by Mg atom and structural optimization of the Mg atom contained structure was done [36]. The Rietveld refinement pattern and difference plot (shown in Fig. 1d) suggest the presence of MgFeTiO_4 (76.52%) as the major phase along with secondary phases like Fe_2TiO_4 (18.45%), FeTiO_3 (5.03%) in the experimental XRD pattern. Crystallographic parameters obtained from Rietveld refinement are tabulated in Table 1. MgFeTiO_4 has a cubic spinel structure corresponding to space group $\text{Fd}3\text{m}$ where

Table 1 Crystallographic data for the Rietveld refinement of MgFeTiO_4

Atom	Wyckoff position	x	y	z	Occupancy site
Mg	16d	0.6250	0.6250	0.6250	0.25
Fe	16d	0.6250	0.6250	0.6250	0.25
Ti	16d	0.6250	0.6250	0.6250	0.5
Mg	8a	0.0000	0.0000	0.0000	0.5
Fe	8a	0.0000	0.0000	0.0000	0.5
O	32e	0.3847	0.3847	0.3847	1

$$a = 0.853 \text{ nm}, R_{\text{exp}} = 1.83, R_{\text{wp}} = 2.79, R_{\text{p}} = 2.02, \text{GOF} = 1.52$$

Ti atoms occupy octahedral sites (16d), while Mg and Fe atoms occupy both octahedral sites (16d) and tetrahedral sites (8a). Oxygen atoms occupy face-centered lattice site (32e). The refined lattice parameters for the cubic spinel are calculated to be $a = 0.853 \text{ nm}$ which matches with the previous reported LiFeTiO_4 [30]. Further, the crystal structure of MgFeTiO_4 spinel is generated by VESTA software using the refined structural parameters and as shown in Fig. 1d.

The MgFeTiO_4 shows a similar structure as LiFeTiO_4 both have spinel framework and same space group $\text{Fd}\bar{3}\text{m}$ (227). Hence, this type of composition forms a spinel structure ABO_4 in which $(\text{Mg}_{1/2} \text{Fe}_{1/2})_{8a} [\text{Mg}_{1/4} \text{Fe}_{1/4} \text{Ti}_{1/2}]_{16d} \text{O}_4$ and without any vacancies. Here tetrahedral and octahedral sites are represented by “()” and “[]”, respectively.

The FTIR spectrum and deconvoluted peaks of calcined MgFeTiO_4 powder are shown in Fig. 2a and b. The vibrational modes of FTIR spectra are tabulated in Table 2. The absorption bands in the range of 4000 cm^{-1} to 1300 cm^{-1} are assigned to O–H stretching vibration as moisture is present in the samples [37, 38]. The characteristic peaks at 1074 and

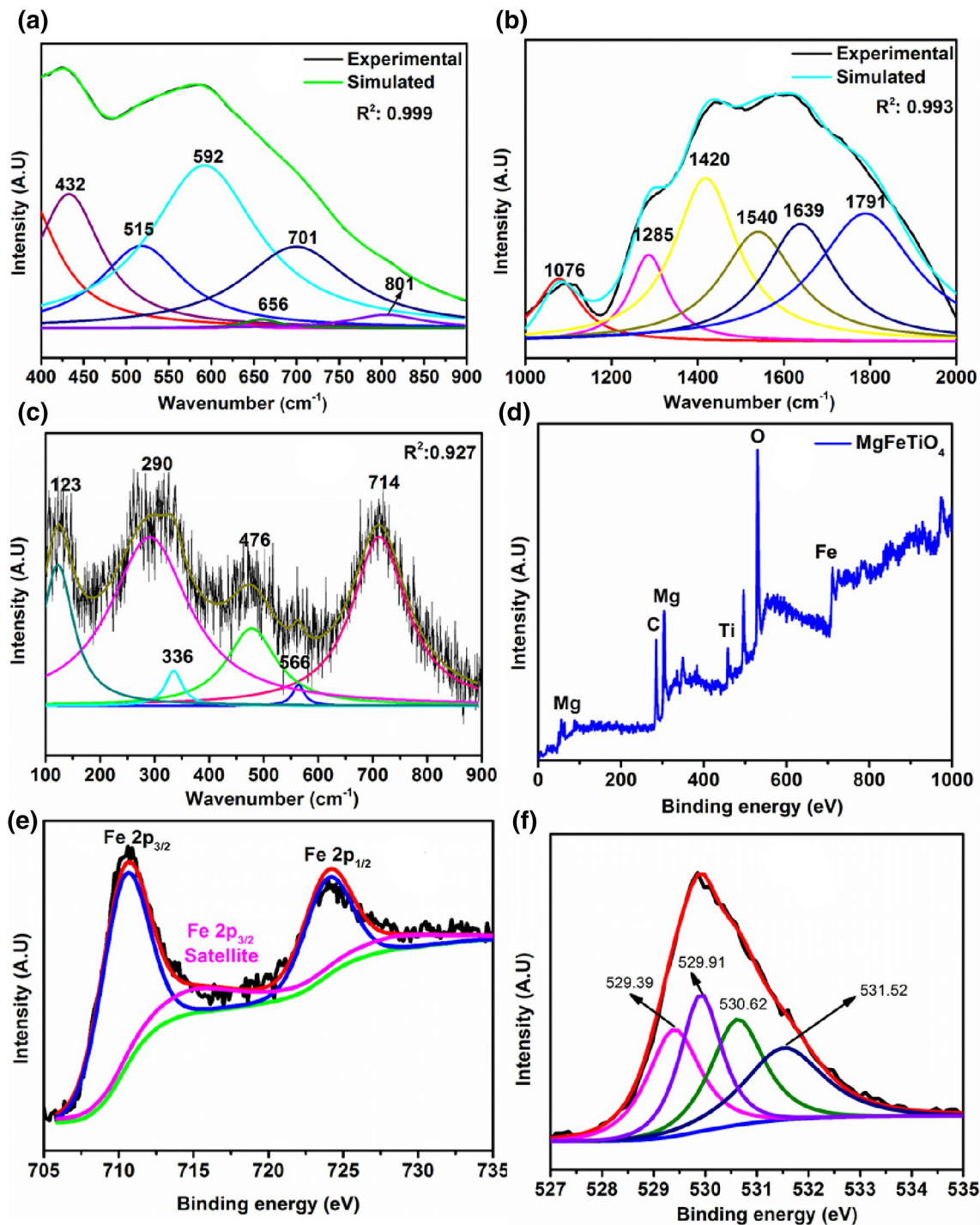


Fig. 2 a, b FTIR spectrum and de-convoluted FTIR peaks of MgFeTiO_4 , c Raman spectrum and deconvoluted Raman peaks of MgFeTiO_4 , XPS plot of MgFeTiO_4 d overall e iron (Fe 2p) f oxygen (O 1s)

Table 2 FTIR of MgFeTiO₄

Wave no. (cm ⁻¹)	Assignment	Refs
432	Mg–O stretching vibration	[38]
515	Ti–O stretching in TiO ₆	[39]
592	Fe–O–Fe tetrahedra vibration mode	[40]
656	FeO ₄ tetrahedra	[39]
701	TiO ₆ in pure phase of Mg ₂ TiO ₄	[39, 40]
801	Ti–O–Ti vibration bonds or stretching bond is Ti–O–Mg	[37]
1074	Ti–O–Ti vibration bonds or stretching bond is Ti–O–Mg	[37]
1383	Deformation of O–H bonds	[32]

Table 3 Raman of MgFeTiO₄

Wave no. (cm ⁻¹)	Assignment	Symmetry species	Refs
122	Lattice mode of vibration	–	[40]
290	Asymmetric stretching vibration of Fe–O bond in FeO ₆ octahedral	<i>E_g</i>	[40]
336	Mg ₂ TiO ₄ spinels and MgO ₄	<i>F_{2g}</i>	[40–42]
476	Mg ₂ TiO ₄ spinels and MgO ₆	<i>F_{2g}</i>	[40–42]
565	Fe–O octahedral bond found in Fe ₂ TiO ₄	<i>F_{2g}</i>	[40]
714	Symmetric stretching of Ti–O bond in TiO ₆ octahedral	<i>A_{1g}</i>	[40–42]

801 cm⁻¹ are assigned to stretching vibration of Ti–O–Mg [37]. The absorption bands corresponding to 656 cm⁻¹ and 701 cm⁻¹ are assigned to the vibration of FeO₄ tetrahedra and TiO₆ octahedra in Mg₂TiO₄ [39, 40]. The characteristic peak at 592 cm⁻¹ is due to the Fe–O–Fe tetrahedra vibration mode [40]. IR spectrum shows broad hump due to the overlapping of different peaks obtained from bond vibration of Fe–O, Ti–O, and Mg–O [32, 39].

The Raman spectrum and deconvoluted peaks of MgFeTiO₄ are shown in Fig. 2c. Different bands in the Raman spectra have been identified and presented in Table 3. Raman spectra confirm that Ti–O, Mg–O, and Fe–O bonds are present in the sample. Five vibrational Raman active modes are present in the spinel structure; *A_{1g}* at (714 cm⁻¹), *E_g* at (290 cm⁻¹), and three *F_{2g}* modes at (336, 476, 566 cm⁻¹) [40]. The study confirms the presence of Mg₂TiO₄ and Fe₂TiO₄ by identifying, respectively, two Mg–O vibration bonds found in Mg₂TiO₄ spinel at 336, 476, and Fe–O vibration bond found in Fe₂TiO₄ at 566 cm⁻¹. The Raman modes conforming to TiO₆ and FeO₆ octahedra were found at 714 and 290 cm⁻¹, respectively [41, 42]. Raman analysis shows that Mg and Fe are present at both tetrahedral (8a) and octahedral (16d) sites; the Rietveld of XRD analysis also supports this.

XPS study of MgFeTiO₄ sample calcined at 950 °C is also done to confirm the valence state of Fe (shown in

Fig. 2d). The XPS spectra are deconvoluted and analyzed the peak by using XPSPEAK 41 software with Lorentzian function and Shirley background. Figure 2d shows the overall XPS spectra of the sample which reveals the existence of Mg, Fe, Ti, and O elements (supports the EDX results in next section). Figure 2e shows Fe 2p spectra and the peaks observed at 710.3 eV and 723.9 eV are the characteristic doublets of Fe 2p_{3/2} and Fe 2p_{1/2}, respectively. Also, a satellite present at 715.0 eV appears due to the presence of FeO in the sample. The results show that Fe has +2 valence state, hence proves that Fe⁺² replaces Mg⁺² ion in the structure forming MgFeTiO₄ is compound [43]. Additionally, Fig. 2f shows O 1s spectrum, the peak at 529.3 and 529.9 is attributed to metal-oxide (Mg/Fe/Ti)–O. The peak at 530.6 and 531.5 can be assigned to hydroxyl group (OH) [44–47].

The morphology and compositional analysis (mapping) of the MgFeTiO₄ sample are done using a scanning electron microscope (SEM). The SEM image, energy dispersive X-ray spectrum (EDS), and mapping of the sample calcined at 950 °C are shown in Fig. 3. The mapping results show a homogenous distribution of Mg, Fe, Ti, and O in the sample (Fig. 3a–d). The EDS results suggest that the prepared sample MgFeTiO₄ consists of 10.01% Mg, 27.11% Fe, 24.59% Ti in weight, giving an atomic ratio of Mg:Fe:Ti to be 1:1:1. The EDS confirms the presence of constituent elements Mg, Fe, Ti, O within the sample, shown in Fig. 3e. The SEM micrograph (Fig. 3f) shows the nanoparticles formation and they are present in agglomerated form due to the high reactivity of nanoparticles. Transmission electron microscope (TEM) and Selected area electron diffraction (SAED) images of MgFeTiO₄ are illustrating in Fig. 4a and b, respectively. The TEM images clarify that nanoparticles are spherical as it is not seen in SEM. The SAED diffraction spots seem to be forming a discontinuous ring, which confirms the polycrystalline nature of the sample. The SAED image shows diffraction spots as planes (311) and (400) and lattice fringes of (311) and (400) can be seen in HRTEM image with spacing 0.271 nm and 0.244 nm. These results also support for XRD analysis.

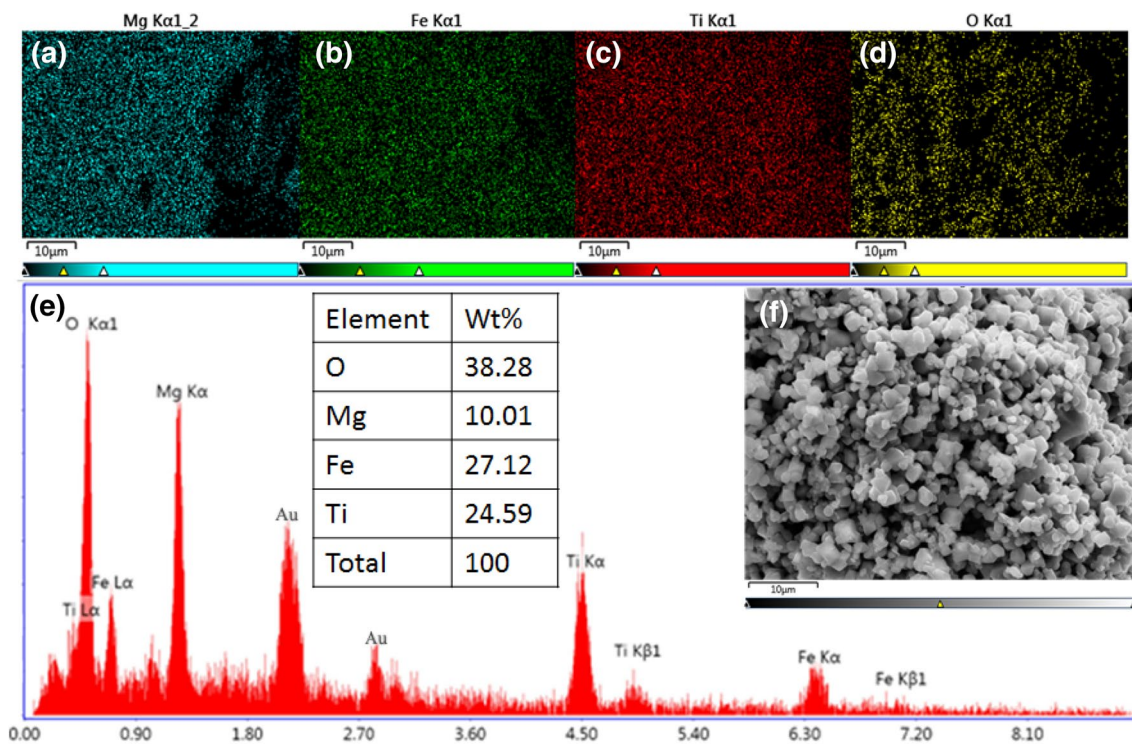


Fig. 3 Morphology and compositional analysis of powder sample

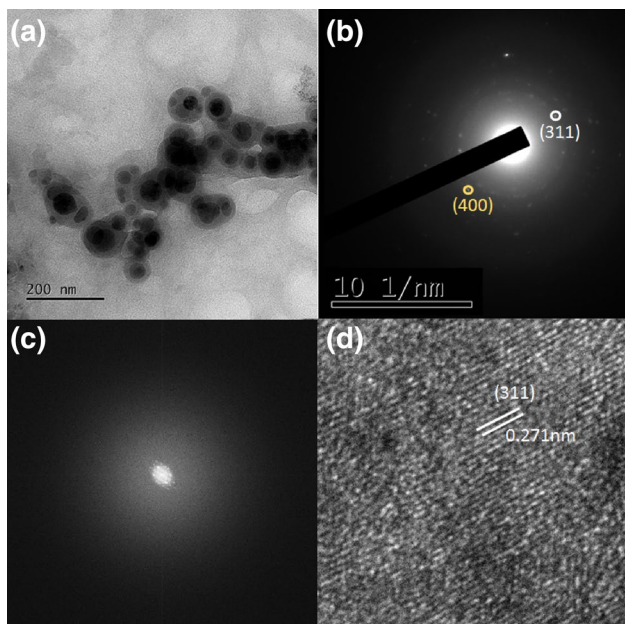


Fig. 4 a TEM, b SAED, c FFT, and d HRTEM analysis of powder sample

3.2 Electrical characteristics

The impedance spectroscopic plots (Nyquist plot) of MgFeTiO₄ are shown in Fig. 5a and b, which reveal the

presence of single semi-circles at all measuring temperature. As the temperature increases, the radius of semi-circles decreases, which can be attributed to the reduction in bulk resistance, relaxation time, and an increase in electrical conductivity of the material. It shows the semiconducting behavior of material [31]. A presence of large single semi-circle is a combination of one or more physical phenomenon of materials like at high-frequency semi-circle is attributed to grain property and low-frequency semi-circle is attributed to grain boundary and/or material–electrode interface properties [48]. For validation, the experimental curve is fitted using ZSimpWin software considering equivalent circuit ($R_g Q_g$)($R_{gb} Q_{gb}$) as shown in Fig. 5c and d. In the equivalent circuit model, R_g and R_{gb} represent the grain and grain boundary resistance, while Q_g and Q_{gb} are grain and grain boundary constant phase element (CPE), respectively [35, 49]. Hence a single semi-circular arc is attributed to the contribution of grain and grain boundary in electrical properties of the material. The CPE is used due to the non-ideal capacitor behaviors [50, 51]. The fitting values are tabulated in Table 4. The resistance is decrease with increase in temperature which shows the negative temperature coefficient of resistance (NTCR)-type behavior that confirms the semi-conducting nature of sample and more free charge carriers (electron/hole) are available for conduction [52].

The real (Z') and imaginary (Z'') part of the impedance spectra, varying with frequency and temperatures (bode

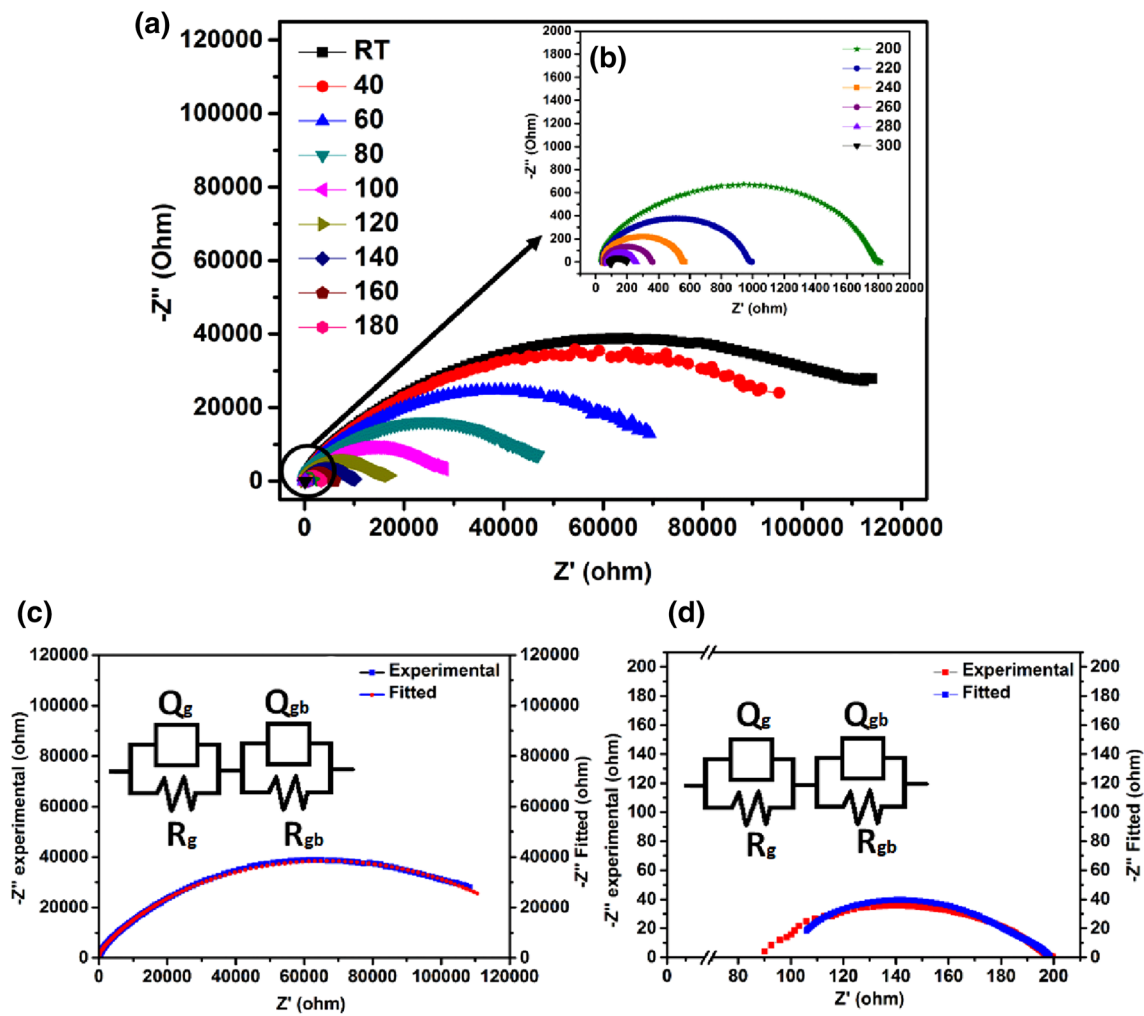


Fig. 5 a Nyquist plot variation with frequency at different temperatures, Fitting of Complex impedance spectroscopic (CIS), and equivalent circuit model of MgFeTiO_4 at different temperatures c Room temperature d 300 °C

Table 4 The fitted equivalent circuit and their parameters at different temperatures

Temp	Circuit	R_g (ohm)	Q_g (nF)	n	R_{gb} (ohm)	Q_{gb} (nF)	n
RT	(RQ)(RQ)	1.03E5	8.56	0.85	1.15E4	1.71	0.93
100	(RQ)(RQ)	2.39E4	8.46	0.82	3076	1.00	0.95
200	(RQ)(RQ)	1767	7.56	0.83	150	10.22	0.81
300	(RQ)(RQ)	103	16.8	0.80	92.17	10.20	0.80

plot), are shown in Fig. 6a and b. The Z' drops with an increase in frequency and temperature which signifies that the conductivity of material increases as the temperature and frequency increase. All the curves merge towards a higher frequency region which indicates the release of space charge due to the diminishing barrier properties of materials [31, 53]. In loss spectrum (frequency vs. Z''), Z'' values increase up to a certain frequency, and after that, it decreases with increase in frequency and temperature. The presence of one peak in a loss spectrum suggests the

existence of a single relaxation process in a material due to space charge relaxation. The space charge relaxation dominates due to the presence of grain and grain boundaries. It is seen that the peak position of Z'' is shifted towards higher frequency region and also peak broadening occurs with an increase in temperature. This peak shift towards a higher frequency side with an increase in temperature establishes an increase in the hopping rate and a decrease in the relaxation time of the mobile charge carriers, thus indicating a rapid motion of mobile carriers. It is

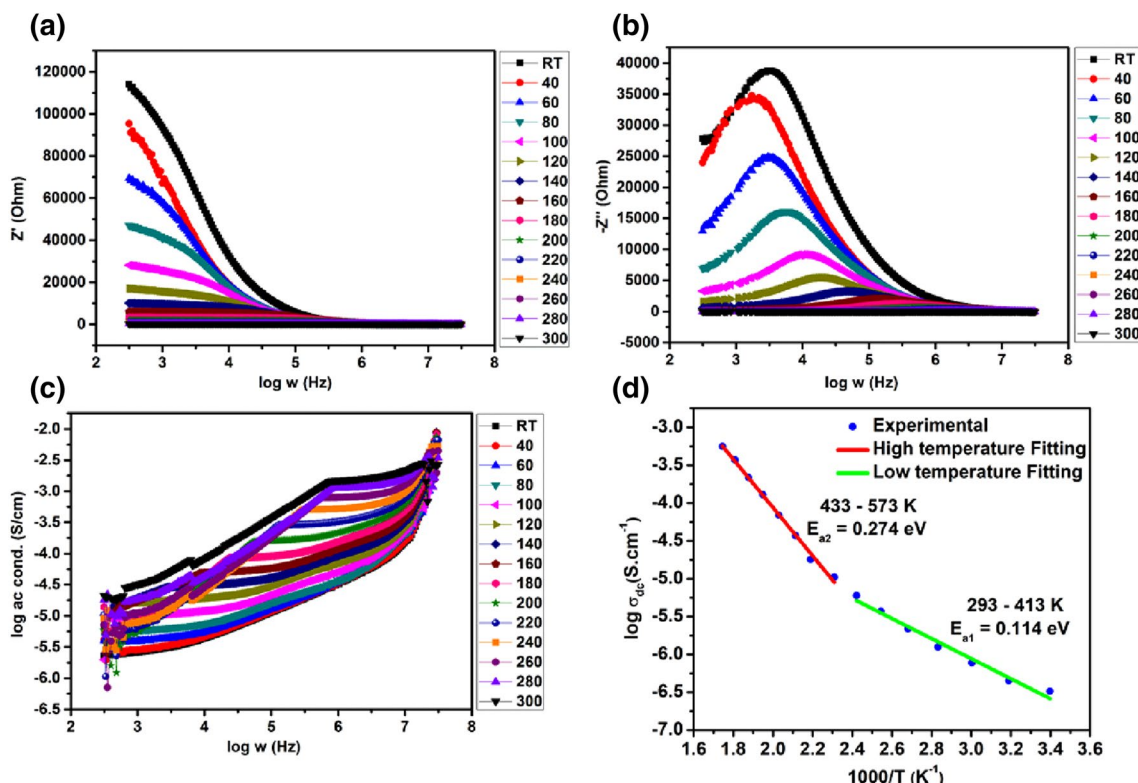


Fig. 6 **a, b** Bode plot, the variation in real impedance (Z') and imaginary impedance (Z'') with frequency at different temperatures **c** ac conductivity plot as a function of temperature **d** the variation between $\log(\sigma_{dc})$ with $1000/T$

also observed that the drop in Z'' maxima with increased temperature results in a loss in resistive property of the sample. The temperature-dependent relaxation process is responsible for the enhanced conductivity in the material [48, 54–56].

Figure 6c shows the ac conductivity with varying frequencies and temperatures. The value of ac conductivity is found out from the following relation:

$$\sigma_{ac} = \omega \epsilon_r \epsilon_0 \tan \delta \tag{2}$$

where ω angular frequency, ϵ_r ; relative permittivity, ϵ_0 ; permittivity of vacuum (8.854×10^{-14} F/cm), $\tan \delta$ dissipation factor, f ; frequency, C ; capacitance of the specimen in Farads, t ; thickness of the specimen, A ; area of the specimen in (sq. cm.). The ω and ϵ_r are calculated by using the formula $\omega = 2\pi f$ and $\epsilon_r = Ct/\epsilon_0 A$, respectively. The ac conductivity is enhanced with an increase in frequency due to change in oxidation state (Fe ions Fe^{2+}/Fe^{3+} , Fe^{3+}/Fe^{4+} , and Ti ions Ti^{3+}/Ti^{4+}) with the creation of Mg vacancies. The hopping process increases due to the increased amount of charge carriers formed by the change in the oxidation state. The material bulk conductivity is estimated from the curve fitted with the experimental data (Fig. 5). The dc conductivity of the material is calculated by using the relation:

$$\sigma_{dc} = l/(R \times A) \tag{3}$$

where R_b ; material bulk resistance, l ; specimen thickness and A ; specimen area. The dc conductivity of the material is found to be 4.61×10^{-7} at room temperature and 5.68×10^{-4} S cm^{-1} at 300 °C. The activation energies (E_{a1} and E_{a2}) are calculated for the two different regions (293–413 K and 433–573 K) and calculated by using the Arrhenius equation,

$$\sigma_{dc} = \sigma_o e^{(-E/kT)} \tag{4}$$

where σ_{dc} ; conductivity, T ; absolute temperature, σ_o ; pre-exponential factor, E ; activation energy for charge transfer and k ; Boltzmann constant. The variation of $\log(\sigma_{dc})$ with $1000/T$ is found to be almost linear (shown in Fig. 6d). The slope of the line helps to determine the activation energy, and it showed that the conductivity is a thermally activated process [31, 57]. The activation energies, $E_{a1} = E_m$ and $E_{a2} = E_f + E_m$ where E_m is the energy required for the migration of charge carriers and E_f is the energy required for the defect formation. The activation energy of the synthesized sample is calculated to be $E_{a1} = 0.114$ eV and $E_{a2} = 0.274$ eV which indicates that charge carries require very less energy to initiate electrical conduction. It is observed that E_{a2} has higher value than E_{a1} which shows at high temperature the

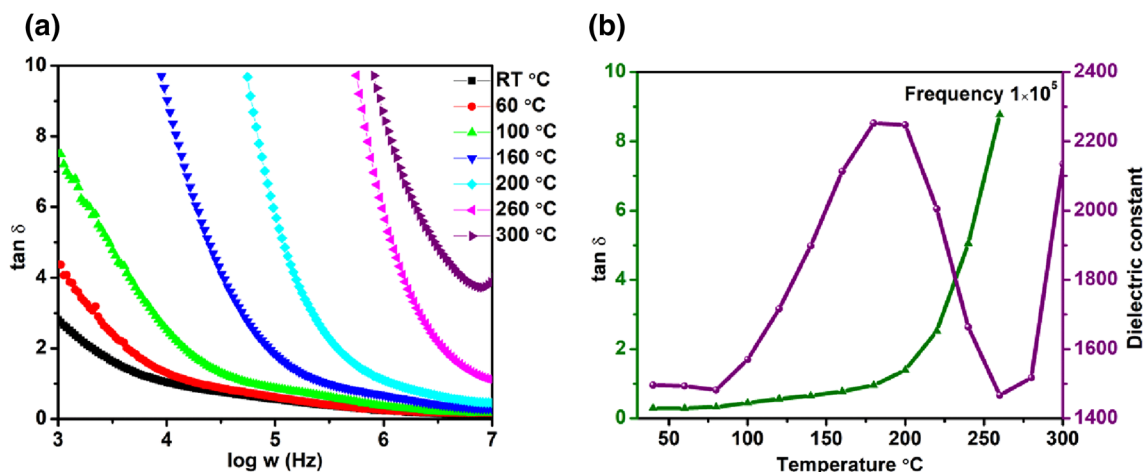


Fig. 7 a Dielectric loss tangent ($\tan \delta$) vs. applied frequency at different temperatures (RT–300 °C) b Dielectric constant and loss vs. temperature

defect formation and migration of charge carriers [58]. The change in activation energy is attributed to change in conduction mechanism. At low temperature the conduction occurs through the hopping of electrons between Fe^{2+} to Fe^{3+} and Ti^{3+} to Ti^{4+} ions. However at higher temperature the conduction occurs by hopping of polarons and confirmed by the higher E_{a2} value than E_{a1} [59].

Figure 7a shows the plot of dielectric loss tangent ($\tan \delta$) vs. applied frequency at different temperatures (RT–300 °C). The $\tan \delta$ decreases with frequency, however, with temperature it increases (Fig. 7b) which shows the thermal activation and accumulation of charge carriers [58, 60]. At lower frequency, the $\tan \delta$ decreases very rapid because low conductivity of grain boundary which required more energy for electron exchange between Fe^{2+} to Fe^{3+} and Ti^{3+} to Ti^{4+} ions as a result loss is high. However, at high frequency $\tan \delta$ becomes constant because it corresponds to high conductivity of grain where a small energy is required for electron transfer [60, 61]. The thermal activation process is also confirmed by dielectric constant value which increases with temperature Fig. 7b.

4 Conclusions

In summary, the spinel structure MgFeTiO_4 is synthesized by a conventional solid-state reaction route. The XRD pattern showed that MgFeTiO_4 is formed along with some presence of other phases like Fe_2TiO_4 , FeTiO_3 , as confirmed by Rietveld analysis. FTIR and Raman spectrum confirmed the presence of Mg_2TiO_4 and Fe_2TiO_4 . The Nyquist plot confirms that grain and grain boundary both contribution occurs in the conduction process of the synthesized material. The variation in dc conductivity 4.61×10^{-7} at RT and

$5.68 \times 10^{-4} \text{ S cm}^{-1}$ at 300 °C, indicates that it is a thermally activated process. The activation energy is calculated in two different temperature-dependent conductivity regions and found to be $E_{a1} = 0.114 \text{ eV}$ (293–413 K) and $E_{a2} = 0.274 \text{ eV}$ (433–573 K).

References

1. L. Qu, D. Luo, S. Fang, Y. Liu, L. Yang, S. Hirano, C.-C. Yang, *J. Power Sour.* **307**, 69 (2016)
2. N.S. Lewis, D.G. Nocera, *Proc. Natl. Acad. Sci.* **103**, 15729 (2006)
3. G.M. Joselin Herbert, S. Iniyan, E. Sreevalsan, S. Rajapandian, *Renew. Sustain. Energy Rev.* **11**, 1117 (2007)
4. A. Mustafa Omer, *Renew. Sustain. Energy Rev.* **12**, 344 (2008)
5. P.G. Bruce, B. Scrosati, J.-M. Tarascon, *Angew. Chem. Int. Ed.* **47**, 2930 (2008)
6. B. Dunn, H. Kamath, J.-M. Tarascon, *Science* **334**, 928 (2011)
7. C. Liu, Z.G. Neale, G. Cao, *Mater. Today* **19**, 109 (2016)
8. X. Sun, V. Duffort, B.L. Mehdi, N.D. Browning, L.F. Nazar, *Chem. Mater.* **28**, 534 (2016)
9. R. Mohtadi, F. Mizuno, *Beilstein J. Nanotechnol.* **5**, 1291 (2014)
10. P. Saha, M.K. Datta, O.I. Velikokhatnyi, A. Manivannan, D. Alman, P.N. Kumta, *Prog. Mater. Sci.* **66**, 1 (2014)
11. W. Li, S. Cheng, J. Wang, Y. Qiu, Z. Zheng, H. Lin, S. Nanda, Q. Ma, Y. Xu, F. Ye, M. Liu, L. Zhou, Y. Zhang, *Angew. Chem. Int. Ed.* **55**, 6406 (2016)
12. H.D. Yoo, I. Shterenberg, Y. Gofer, G. Gershinsky, N. Pour, D. Aurbach, *Energy Environ. Sci.* **6**, 2265 (2013)
13. J. Muldoon, C.B. Bucur, A.G. Oliver, T. Sugimoto, M. Matsui, H.S. Kim, G.D. Allred, J. Zajicek, Y. Kotani, *Energy Environ. Sci.* **5**, 5941 (2012)
14. S. Rasul, S. Suzuki, S. Yamaguchi, M. Miyayama, *Electrochim. Acta* **82**, 243 (2012)
15. Y. Li, Y. Nuli, J. Yang, T. Yiliner, J. Wang, *Chin. Sci. Bull.* **56**, 386 (2011)
16. A.B. Ikhe, N. Naveen, K.S. Sohn, M. Pyo, *Electrochim. Acta* **283**, 393 (2018)

17. E. Levi, G. Gershinsky, D. Aurbach, O. Isnard, G. Ceder, *Chem. Mater.* **21**, 1390 (2009)
18. D. Aurbach, Z. Lu, A. Schechter, Y. Gofer, H. Gizbar, R. Turge- man, Y. Cohen, M. Moshkovich, E. Levi, *Nature* **407**, 724 (2000)
19. E. Levi, Y. Gofer, D. Aurbach, *Chem. Mater.* **22**, 860 (2010)
20. D. Aurbach, G.S. Suresh, E. Levi, A. Mitelman, O. Mizrahi, O. Chusid, M. Brunelli, *Adv. Mater.* **19**, 4260 (2007)
21. A. Mitelman, M.D. Levi, E. Lancry, E. Levi, D. Aurbach, *Chem. Commun.* **41**, 4212 (2007)
22. J.P. Pereira-Ramos, R. Messina, J. Perichon, *J. Electroanal. Chem. Interfacial Electrochem.* **218**, 241 (1987)
23. P. Novak, R. Imhof, O. Haas, *Electrochim. Acta* **45**, 351 (1999)
24. Z. Feng, J. Yang, Y. NuLi, J. Wang, *J. Power Sour.* **184**, 604 (2008)
25. Y. NuLi, Y. Zheng, Y. Wang, J. Yang, *J. Mater. Chem.* **21**, 12437 (2011)
26. M.A. Arillo, M.L. López, E. Perez-Cappe, C. Pico, M.L. Veiga, *Solid State Ionics* **107**, 307 (1998)
27. M.V. Reddy, G.V. Subba Rao, B.V.R. Chowdari, *Chem. Rev.* **113**, 5364 (2013)
28. U. Sen, S. Sarkar, P. Veluri, S. Singh, S. Mitra, *Nanosci. Nano- technol Asia* **3**, 21 (2013)
29. S. Kumar, R. Kumar, B. Koo, H. Choi, *J. Ceram. Soc. Jpn* **117**, 689 (2009)
30. S. Chakrabarti, A.K. Thakur, K. Biswas, *Solid State Ionics* **262**, 49 (2014)
31. V.D. Nithya, R. Kalai Selvan, *Phys. B Condens. Matter* **406**, 24 (2011)
32. B. Mandal, A.K. Thakur, *Ionics (Kiel)* **24**, 1065 (2018)
33. R.K. Bhuyan, T.S. Kumar, D. Goswami, A.R. James, A. Perumal, D. Pamu, *Mater. Sci. Eng. B Solid State Mater. Adv. Technol.* **178**, 471 (2013)
34. S.H. Yang, Y.C. Hung, P.C. Tseng, H.Y. Lee, *J. Alloys Compd.* **801**, 394 (2019)
35. L. Vijayan, R. Cheruku, G. Govindaraj, *Mater. Res. Bull.* **50**, 341 (2014)
36. S. Chakrabarti, A.K. Thakur, K. Biswas, *J. Power Sour.* **313**, 81 (2016)
37. C.H. Ashok, V.K. Rao, C.H. Chakra, *J. Nanomed. Nanotechnol.* **06**, 2 (2015)
38. L.-X. Li, D. Xu, X.-Q. Li, W.-C. Liu, Y. Jia, *New J. Chem.* **38**, 5445 (2014)
39. P. Tarte, R. Cahay, A. Garcia, *Phys. Chem. Miner.* **4**, 55 (1979)
40. S. Chakrabarti, A.K. Thakur, K. Biswas, *Ionics (Kiel)* **22**, 2045 (2016)
41. A.V. Knyazev, M. Mączka, I.V. Ladenkov, E.N. Bulanov, M. Ptak, *J. Solid State Chem.* **196**, 110 (2012)
42. Z. Wang, S.K. Saxena, C.S. Zha, *Phys. Rev. B* **66**, 024103 (2002)
43. J. Jayabharathi, A. Prabhakaran, C. Karunakaran, V. Thanikachal- lam, M. Sundharesan, *RSC Adv.* **6**, 18718 (2016)
44. J.L. Gautier, E. Rios, M. Gracia, J.F. Marco, J.R. Gancedo, *Thin Solid Films* **311**, 51 (1997)
45. N. Huo, Y. Yin, W. Liu, J. Zhang, Y. Ding, Q. Wang, Z. Shi, S. Yang, *New J. Chem.* **40**, 7068 (2016)
46. Y. Sharma, N. Sharma, G.V.S. Rao, B.V.R. Chowdari, *Electrochim. Acta* **53**, 2380 (2008)
47. Y. Sharma, N. Sharma, G.V. Subba Rao, B.V.R. Chowdari, *Solid State Ionics* **179**, 587 (2008)
48. S. Dutta, R.N.P. Choudhary, P.K. Sinha, A.K. Thakur, *J. Appl. Phys.* **96**, 1607 (2004)
49. R. Cheruku, G. Govindaraj, L. Vijayan, *Mater. Chem. Phys.* **141**, 620 (2013)
50. R. Cheruku, L. Vijayan, G. Govindaraj, *Mater. Sci. Eng. B Solid State Mater. Adv. Technol.* **177**, 771 (2012)
51. L. Vijayan, R. Cheruku, G. Govindaraj, S. Rajagopan, *Mater. Chem. Phys.* **130**, 862 (2011)
52. J.R. Ferna, P. La, J. Gutie, *Mater. Res. Bull.* **47**, 1861 (2012)
53. A. Shukla, R.N.P. Choudhary, A.K. Thakur, D.K. Pradhan, *Phys. B Condens. Matter* **405**, 99 (2010)
54. M. Azizar Rahman, A.K.M. Akther Hossain, *Phys. Scr.* **89**, 025803 (2014)
55. R. Martínez, A. Kumar, R. Palai, J.F. Scott, R.S. Katiyar, *J. Phys. D Appl. Phys.* **44**, 105302 (2011)
56. D. Sekulic, Z. Lazarevic, C. Jovalekic, A. Milutinovic, N. Rom- cevic, *Sci. Sinter.* **48**, 17 (2016)
57. M. Ram, *Solid State Sci.* **12**, 350 (2010)
58. O. Padmaraj, M. Venkateswarlu, N. Satyanarayana, *Ceram. Int.* **41**, 3178 (2015)
59. A. Ashok, T. Somaiah, D. Ravinder, C. Venkateswarlu, C.S. Reddy, K.N. Rao, M. Prasad, *World J. Condens. Matter Phys.* **02**, 257 (2012)
60. N. Singh, A. Agarwal, S. Sanghi, S. Khasa, *J. Magn. Magn. Mater.* **324**, 2506 (2012)
61. A. Ray, P. Maji, A. Roy, S. Saha, P. Sadhukhan, S. Das, *Mater. Res. Express* **6**, 12504 (2020)

Publisher's Note Springer Nature remains neutral with regard to jurisdictional claims in published maps and institutional affiliations.